RESEARCH ARTICLE

Quantification of Marangoni flows and film morphology during solid film formation by inkjet printing

Hirotaka Ishizuka[1] · Jun Fukai[1]

Abstract

We visualized experimentally the internal flow inside inkjet droplets of polystyrene–anisole solution during solid film formation on substrates at room temperature. The effects of contact angle and evaporation rate on the internal flow and film morphology were quantitatively investigated. The transport process during film formation was examined by measuring the relationship between internal flow and film morphology, which provided three remarkable findings. First, self-pinning and the strength of outward flow on the free surface under 2.3 Pa s determined film morphology. The solute distribution, corresponding to rim areas in ring-like films and a convex trough in dot-like films, had already developed at self-pinning. Second, the mass fraction at self-pinning close to the contact line converged to one, regardless of the film morphology. This implies that self-pinning is independent of parameters such as the contact angle and evaporation rate. Third, at room temperature, the solutal Marangoni numbers were 20–30 times larger than the thermal ones. Thus, the outward flow on the free surface caused by the solutal Marangoni effect dominates in droplets before self-pinning. The solutal Marangoni number at self-pinning and thickness variation at the center of the film displayed a good relationship for droplets with different contact angles and evaporation rates. This suggests that film morphology can be technically controlled by solutal Marangoni number at room temperature.

1 Introduction

Solid formation by inkjet printing has been widely investigated, and attempts have been made to scale this technique to allow mass production of color filters for liquid crystal displays and light-emitting layers of organic light-emitting diodes. Inkjet printing is also attractive for other applications, such as solar cells (Cummins and Desmulliez 2012) and biosensing devices (Komuro et al. 2013), that use colloidal inks containing functional materials like nanoparticles.

The evaporation of single colloidal and solution droplets on substrates, which is essential in inkjet printing, has also attracted considerable attention. A variety of solution and colloidal droplets result in different deposit morphologies on substrates, as reviewed by Sefiane (2014), Larson (2014), and Sun et al. (2015). Deposit morphologies vary because of internal flows caused by Marangoni effects and

the coffee-ring effect (Deegan et al. 1997, 2000). To develop a guide for the technical control of deposit morphology as a final goal, the aim of this study was to clarify the effects of contact angle and evaporation rate on the internal flows inside droplets and resultant deposit morphologies.

With respect to colloidal droplets, in the 1980s, Yang and co-workers (Su et al. 1988; Zhang and Yang 1983) visualized the thermal Marangoni flows inside different kinds of organic solvent droplets (wetting diameter = ~ 5 mm) on glass substrates with a temperature gradient. They observed several flow patterns, including Bénard cells. More recently, Hu and Larson (2006) experimentally and numerically studied thermal Marangoni convection in colloidal droplets of water and octane (wetting diameter ≥ 2 mm). They revealed that quantitatively strong inward flow induced by the thermal Marangoni effect restrained the ring-like deposition morphology. Bhardwaj et al. (2009) studied phenomenologically the particle deposition process in water droplets on a glass substrate (wetting diameter = 461 μm) and isopropanol droplets on a polydimethylsiloxane substrate (wetting diameter = 874 μm). Ring- and dot-like deposition morphologies compared well experimentally and numerically. The thermal Marangoni number is considered an independent parameter

✉ Jun Fukai
  jfukai@chem-eng.kyushu-u.ac.jp

1 Department of Chemical Engineering, Graduate School
   of Engineering, Kyushu University, 744 Motooka, Nishi-ku,
   Fukuoka, Fukuoka 819-0395, Japan

to technically control the deposit morphology resulting from colloidal droplets.

Regarding solution droplets, Kajiya et al. (2008) observed the evaporation of polystyrene (PS)–anisole droplets with a constant wetting diameter of 2 mm using fluorescence microscopy. They explained the formation process of a ring-like film by considering the internal flow, which was acquired from the vertically averaged concentration in the radial direction measured from fluorescence intensity. Fukai's group studied the internal flow in polymer solution droplets experimentally and numerically (Fukai et al. 2006; Kaneda et al. 2007; Yasumatsu et al. 2012). In one study, they experimentally investigated the effects of the substrate temperature, evaporation rate, and initial solute concentration on the contact line recession and film morphology during the evaporation of inkjet droplets. They also analyzed numerically the effects of these parameters, as well as the initial droplet diameter and contact angle, on the Marangoni flows inside inkjet droplets.

Experimental visualization inside inkjet droplets of polymer solution has not yet been reported. Because the internal flow inside a droplet of millimeter size is not always analogous to that inside inkjet droplets, the relationship between the final film morphology observed experimentally and the numerically simulated internal flow is not yet clearly understood. In this study, the internal flow inside PS–anisole droplets that are ejected onto solid substrates by the inkjet method is experimentally visualized at room temperature. The internal flow and film morphology are examined at different contact angles and evaporation rates. The transport process in evaporating droplets throughout film formation is quantitatively explained by the relationships between the internal flow, change of average mass fraction over time, and film morphology. Solutal and thermal Marangoni flows and film morphology are quantitatively correlated to evaluate the factors that control film morphology.

2 Experimental methods

Solutions of PS (M.w. = 250,000 g/mol) in anisole were used for inkjet printing. The initial mass fraction of PS $c_{A,0}$ was 0.03. Tracer particles of the light-emitting polymer poly[2,5-bis(3,7-dimethyloctyloxy)-1,4-phenylene-vinylene] (MDMO-PPV, M.w. > 50,000 g/mol; density = 940 kg/m³) were used to visualize the internal flow in the droplets. MDMO-PPV has a fibrous morphology and partially dissolves in PS–anisole to give tracer particles with a size of about a few micrometers. The initial mass fraction of MDMO-PPV was 5×10^{-5}; thus, the addition of MDMO-PPV into the PS–anisole droplets did not affect the temporal variation of the contact angle or wetting diameter of the droplets during evaporation. Perfluorohexylethyltrimethoxysilane

$[R_f, CF_3(CF_2)_5CH_2CH_2Si(OCH_3)_3]$ and n-decyltriethoxysilane $[R_h(C10), CH_3(CH_2)_9Si(OC_2H_5)_3]$ monolayers were prepared on transparent glass substrates by a chemical vapor adsorption method (Morita et al. 2005). Table 1 shows the static contact angle Ψ_S, static receding contact angle Ψ_R, and static advancing contact angle Ψ_A of the PS–anisole droplets ($c_{A,0} = 0.03$; $d_0 = \sim 2.1$ mm) on $R_h(C10)$ and R_f surfaces measured using the inclined plane method.

Figure 1 shows a schematic of the experimental setup. All experiments were carried out at room temperature. The surface temperature of the substrate was maintained at 298 ± 1 K using an isothermal water bath and the atmospheric temperature was maintained at 298 ± 1 K using an air conditioner. The inkjet generator was built in-house. Droplets were ejected from a φ50-μm orifice. The initial droplet diameter d_0 was controlled at 104 ± 5 μm by adjusting the waveform and voltage applied to a piezoceramic actuator placed in the generator. This initial droplet diameter is larger than that used in commercial printers; nevertheless, it is compatible with practical use considering the pixel volume of larger display panels, e.g., 52 or 62 inches. The evaporation rate of the solvent was controlled by adjusting the distance between the nozzle and substrate because the partial pressure of the solvent around the droplet was sensitive to the width of this clearance. Side and top views of droplets deposited on substrates were recorded using charge-coupled device (CCD) cameras at a frame rate of 30 fps. The bottom-view camera was attached to a fluorescence microscope (Nikon, TE2000). The image quality of these cameras is 720×480 dpi. The accuracy of the measurement from the side- and bottom-views are about 1.0 and 0.7 μm/pixel. MDMO-PPV tracer particles inside each droplet were visualized through the microscope and recorded. The center of the wetting area was taken as the origin to allow the positions of the fluorescence tracer particles to be satisfactorily measured. Radial velocity was calculated as the derivative of particle position. The evaporation time t was set to zero when each droplet came in contact with the surface of the substrate. The droplet shape was fitted as spherical cap (circle) from the side-view. The instantaneous wetting diameter d_c and height of each droplet were measured from side-view images. The wetting diameter was also confirmed by the wetting area from the bottom-view. The contact angle Ψ_c, average evaporation rate, described in the next section, and average PS mass fraction c_{av} were then calculated. After

Table 1 Contact angles of PS–anisole droplets (average PS mass fraction $c_{av} = 0.03$) on $R_h(C10)$ and R_f surfaces

Surface	$\Psi_S[°]$	$\Psi_R[°]$	$\Psi_A[°]$
$R_h(C10)$	38.3 ± 0.5	38.2 ± 1.0	41.1 ± 0.7
R_f	73.0 ± 1.5	61.6 ± 2.0	73.5 ± 0.4

Fig. 1 Schematic diagram of the experimental setup
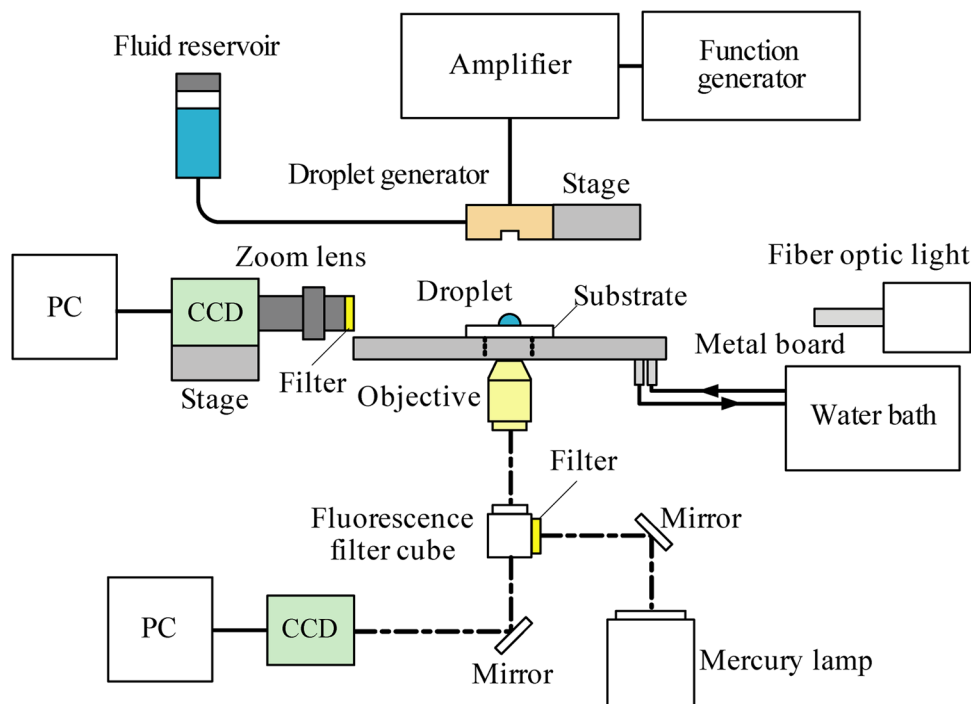
natural drying, three-dimensional profiles of PS films were obtained using a laser microscope (Keyence, VK-8500).

3 Results and discussion

3.1 Evaporation process

Regarding the basic characteristics of the drying processes on the different surfaces, Fig. 2 shows the representative time variation of Ψ_c and the normalized wetting diameter $d_c/d_{c,0}$ of PS–anisole droplets on R_h(C10) and R_f surfaces. In the case of the R_h(C10) surfaces, Ψ_c initially decreased with a constant $d_c/d_{c,0}$. As soon as Ψ_c decreased by evaporation to less than the static receding contact angle, $d_c/d_{c,0}$ decreased and Ψ_c was almost constant. Thereafter, the contact line was fixed because of self-pinning (Deegan et al. 1997, 2000), that is, Ψ_c decreased with a constant $d_c/d_{c,0}$. Finally, PS was deposited on the substrate. In the case of the R_f surfaces, $d_c/d_{c,0}$ decreased immediately while Ψ_c remained almost constant. The evaporation process corresponding to Ψ_c hysteresis was not observed, similar to the reported behavior for PS–xylene droplets on R_f surfaces (Kaneda et al. 2007). After self-pinning occurred, Ψ_c decreased and $d_c/d_{c,0}$ remained constant. The recession of the contact line with almost constant Ψ_c dominated the evaporation process before self-pinning even on R_h(C10) surfaces.

The droplets on R_h(C10) surfaces normally evaporated faster than those on R_f surfaces, because the evaporation volume rate increases with decreasing Ψ_c. When a droplet
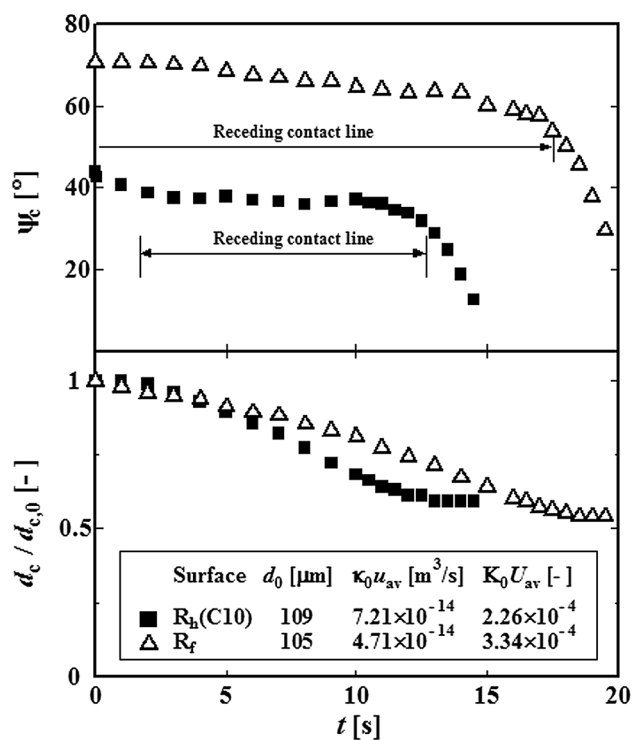

Fig. 2 Time dependence of the contact angle Ψ_c and normalized wetting diameter $d_c/d_{c,0}$ of PS–anisole droplets on R_h(C10) and R_f surfaces

on a substrate evaporates with a constant Ψ_c, the average evaporation volume rate is defined as $\kappa_0 u_{av}$. κ is the function of droplet diameter d and Ψ_c geometrically given by

Eq. (1), which is the ratio of the wetting diameter to the droplet volume.

$$\kappa = \frac{\pi}{4}d^2 \frac{\sqrt[3]{4(1 - \cos \Psi_c)^2 (2 + \cos \Psi_c)}}{\sqrt{(1 - \cos \Psi_c)(1 + \cos \Psi_c)}}. \tag{1}$$

Meanwhile, u_{av} is the receding velocity and equal to $(d_{c,0} - d_{c,pin})/t_{pin}$, where t_{pin} is the time at self-pinning. The initial evaporation volume rate, $\kappa_0 u_{av}$, where $d = d_0$ in Eq. (1), is normalized as $K_0 U_{av} = \kappa_0 (u_{av}/v_0)/(\pi d_0^3/6)$ to consider the effect of the initial droplet diameter. The characteristic velocity v_0 is given by $\mu_0/(\rho_0 d_0)$, where μ_0 is initial viscosity and ρ_0 is initial density. In Fig. 2, since the initial evaporation volume rate $\kappa_0 u_{av}$ or normalized evaporation volume rate $K_0 U_{av}$ of the droplet on R_h(C10) surfaces is about 3/2 times larger than that on R_f, consequently the total evaporation time of the droplet on R_f surfaces is approximately 3/2 times longer than that on R_h(C10) surfaces. Thus, the evaporation times on the different surfaces, $K_0 U_{av}$, should be used to compare the evaporating droplets on different surfaces.

3.2 Marangoni effects on internal flow

The internal flow inside PS–anisole droplets on R_h(C10) and R_f surfaces during evaporation to form solid films was examined. Figure 3 shows an example of internal flow visualization inside PS–anisole droplets on an R_h(C10) surface ($\Psi_s = 38.3°$). Figure 3a shows an instantaneous fluorescence image. A number of fluorescence images in the noted period ($t = 2.3–5.3$ s) were layered; accordingly, the path lines of fluorescent particles are clearly visualized in Fig. 3b. The CCD cameras were focused on the contact line before recording. Tracer particles moving from the top to the bottom of the droplet appeared in focus, whereas those moving in the opposite direction appeared out of focus. Thus, the direction of internal flow could be determined. A schematic of path lines with their direction obtained from the layered image and also by tracking particles positions is presented in Fig. 3c.

Figure 4 shows the typical results of internal flow visualization inside PS–anisole droplets with different Ψ_c and $K_0 U_{av}$. The internal flows are quantitatively compared in the following section. In Fig. 4a, for a PS–anisole droplet on an R_h(C10) surface ($\Psi_s = 38.3°$), at $t = 0–0.4$ s, inward flow on the free surface and outward flow near the bottom of the droplet were observed. At $t = 0.4–4.0$ s, the inward flow became weak near the contact line and there was outward flow on the free surface, while the inward flow in the middle of the droplet still remained. At $t = 7.0–10.0$ s, the outward flow on the free surface became large, and circular flow fully developed inside the droplet. As evaporation proceeded, at $t = 16.0–19.0$ s, the outward flow gradually became weak. In the final stage of evaporation, at $t = 27.0–30.0$ s, the outward flow got further weak before self-pinning at around $t = 30.0$ s. In the case of Fig. 4b, where the droplet evaporated at about twice the rate as that in Fig. 4a, a similar change in the internal flow direction from inward to outward on the free surface was observed. Figure 4c reveals that for a PS–anisole droplet on an R_f surface ($\Psi_s = 73.0°$), at $t = 0–0.4$ s and $0.4–3.5$ s, strong inward flow was observed on the free surface. At $t = 3.5–7.0$ s, the inward flow continuously weakened. At $t = 7.0–10.5$ s, outward flow on the free surface started to develop. Finally, at $t = 10.5–14.0$ s, the outward flow got too weak not to continue after self-pinning at around $t = 14.0$ s.

The change in the internal flow direction from inward to outward on the free surface was commonly observed for the PS–anisole droplets on surfaces with Ψ_s of 38.3° and 73.0°. This change of internal flow in PS–anisole droplets is most likely caused by both thermal and solutal Marangoni effects. Yasumatsu et al. (2012) numerically calculated solutal and thermal Marangoni flows in inkjet droplets of PS–anisole on substrates heated in the range of 313–353 K, and considered the effect of contact angle and initial droplet diameter on flow behavior. According to their findings, the inward flow on the free surface was strongly developed by the thermal Marangoni effect in the early stage of droplet evaporation. Next, the outward flow on the free surface was gradually generated by the solutal Marangoni effect from the contact line and fully developed toward the droplet apex at the end of

Fig. 3 **a** Fluorescence image, **b** path lines, and **c** path lines with flow direction in a PS–anisole droplet on an R_h(C10) surface. In **c**, the solid and dashed lines are the positions of the contact line at the beginning and end of the interval, respectively
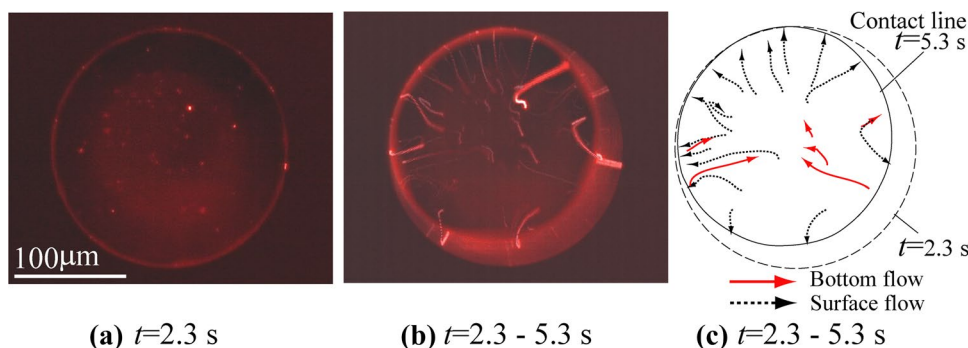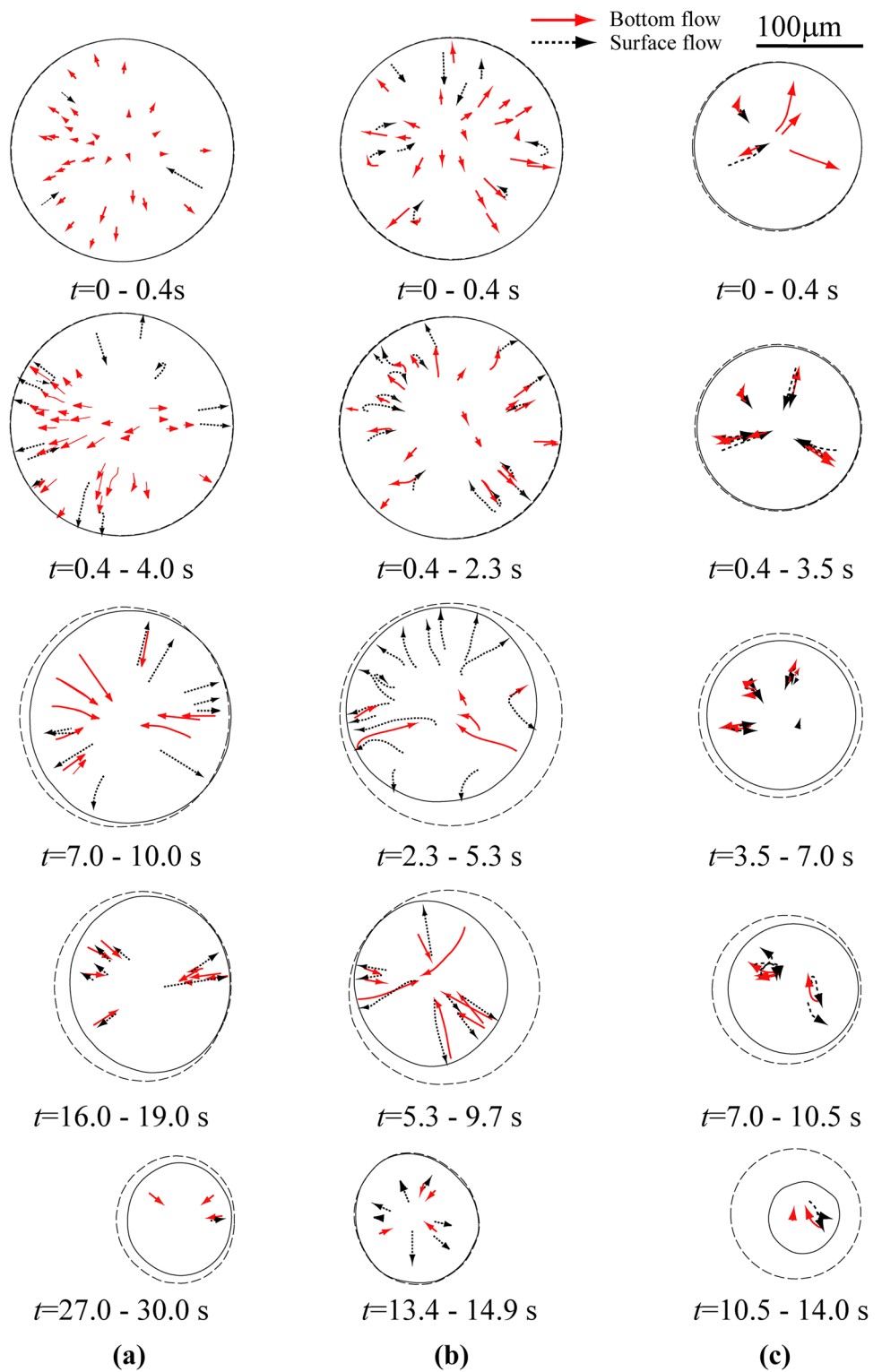

100µm

Contact line
t=5.3 s

t=2.3 s

→ Bottom flow
······▶ Surface flow

(a) t=2.3 s   **(b)** t=2.3 - 5.3 s   **(c)** t=2.3 - 5.3 s

Fig. 4 Internal flow variations in PS–anisole droplets. **a** R_h(C10) surface, $\Psi_s = 38.3°$, $K_0 U_{av} = 1.64 \times 10^{-4}$, $d_0 = 108$ μm, **b** R_h(C10) surface, $\Psi_s = 38.3°$, $K_0 U$av $= 3.34 \times 10^{-4}$, $d_0 = 109$ μm, **c** R_f surface, $\Psi_s = 73.0°$, $K_0 U_{av} = 2.61 \times 10^{-4}$, $d_0 = 101$ μm

evaporation. The surface tension effects of temperature and concentration are largest at the apex and contact line, respectively, while the mass diffusivity is much smaller than the thermal diffusivity in room temperature. The outward flow caused by the solutal Marangoni effect becomes dominant over the inward flow induced by the thermal Marangoni effect with decreasing substrate temperature and Ψ_c.

Kaneda et al. (2008) investigated experimentally and numerically the internal flow inside 0.03 kg/kg PS–anisole droplets of $d_0 \approx 1$ mm on R_f surfaces at room temperature.

They concluded not only solutal Marangoni but also Rayleigh instability initiated the outward flow on the free surface. The internal flow variation of millimeter size droplets is different from that in inkjet droplets. The effect of Rayleigh instability on the internal flow in inkjet droplets, even $d_0 \approx 100$ μm, must be negligible.

3.3 Film formation mechanism

The internal flow velocities are quantitatively compared against the average mass fraction and resultant film morphologies to explore the transport process during film formation. Figure 5a–c shows the radial velocities profiles u_R, which were quantified from the results in Fig. 4a–c, respectively,
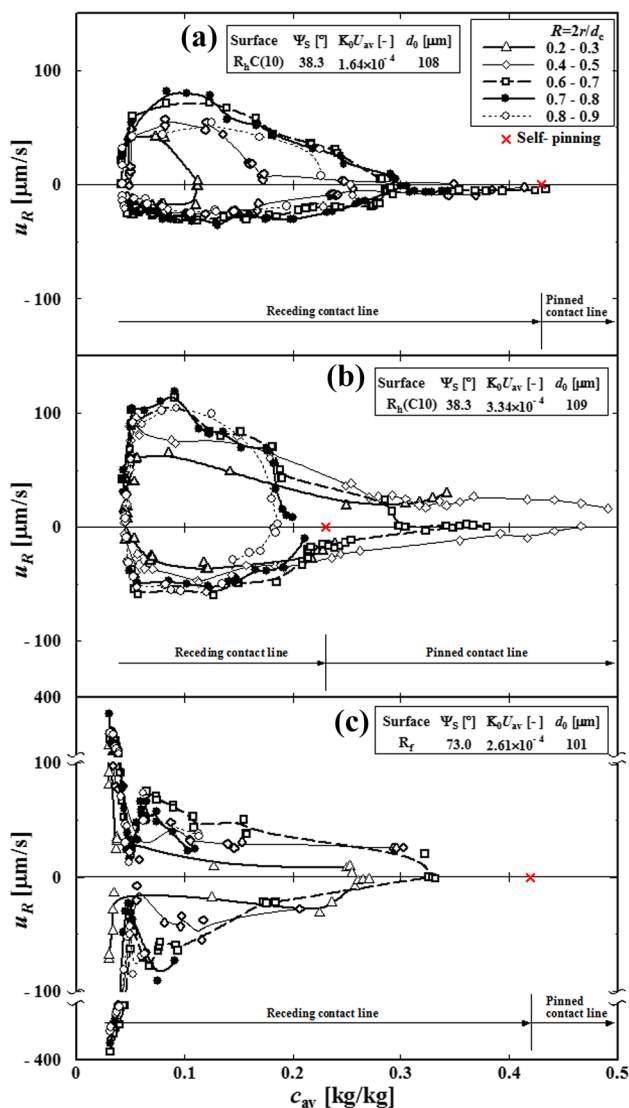
as a function of average mass fraction. The center of the wetting area is taken as the origin, r is set as the radial distance. $R (= 2r/d_c)$ is the normalized radial distance during contact line recession. The absolute accuracy of the measurement is 5 μm/s. Figure 6a–c compares the measured film profiles for the droplets in Fig. 5a–c, respectively, and spherical caps calculated from $d_{c,pin}$ and solute volume. The spherical cap with $d_{c,pin}$ is one of the dot-like morphologies that the droplets formed with no mass transfer after self-pinning when $c_A \geq c_{av,pin}$.

Figure 5a displays the radial velocity profiles of the droplet on R_h(C10) surfaces resulting in the dot-like film shown in Fig. 6a. The outward flow induced by the solutal Marangoni effect has started to develop, so the absolute value of the radial flow velocity on the free surface is larger than that near the bottom of the droplet. The radial flow velocity is the
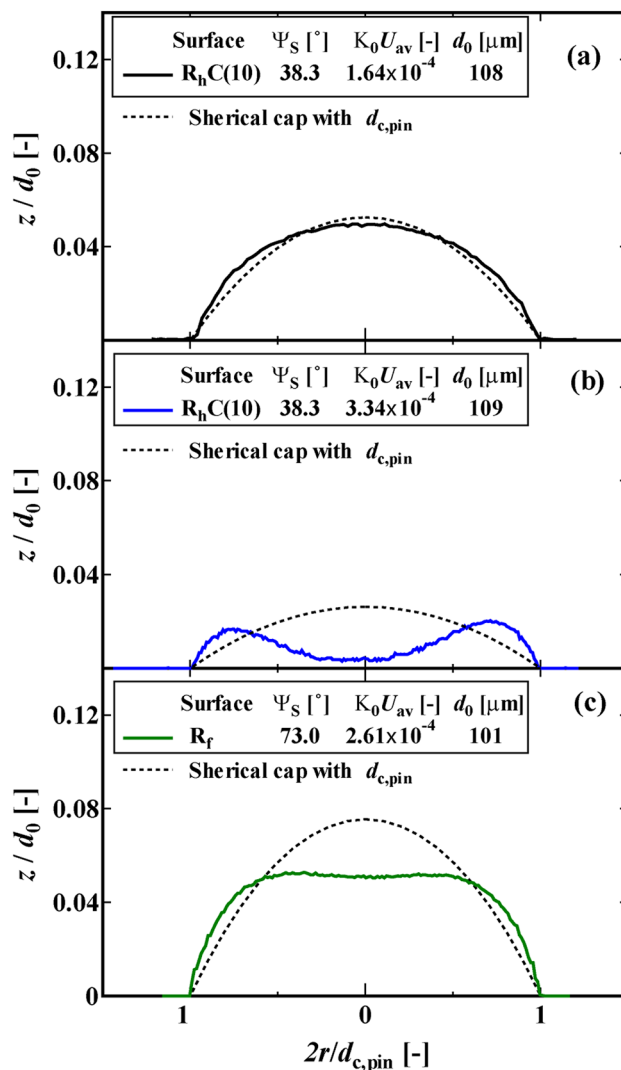

Fig. 5 Radial velocity u_R as a function of average PS mass fraction c_{av}. **a** R_h(C10) surface, $\Psi_s = 38.3°$, $K_0 U_{av} = 1.64 \times 10^{-4}$, $d_0 = 108$ μm, **b** R_h(C10) surface, $\Psi_s = 38.3°$, $K_0 U_{av} = 3.34 \times 10^{-4}$, $d_0 = 109$ μm, **c** R_f surface, $\Psi_s = 73.0°$, $K_0 U_{av} = 2.61 \times 10^{-4}$, $d_0 = 101$ μm

Fig. 6 Profiles of measured PS films on R_h(C10) and R_f surfaces, and spherical caps geometrically calculated using $d_{c,pin}$ and solute volume

largest around $c_{av} = 0.1$. Then, the radial flow velocity starts to decrease in the middle ($0.2 < R < 0.3$) toward the contact line ($0.8 < R < 0.9$) with increasing average mass fraction. At $c_{av} \leq 0.3$, the internal flow velocity was under 5 µm/s, so it was too small to measure. Figure 6a reveals that there is little difference between the measured film profiles and spherical cap. At $c_{av} = 0.3$, the overall flow velocity was already under 5 µm/s; thus, the solute distribution did not change at $0.3 \leq c_{av}$, before self-pinning. The film morphology or solute distribution correlated reasonably well with the profiles of flow velocity against average mass fraction.

Figure 5b presents the radial velocity profiles of a droplet on an R_h(C10) surface resulting in the ring-like film morphology shown in Fig. 6b. The average evaporation volume rate of the droplet in Fig. 5b was about twice that of the one in Fig. 5a; accordingly, the flow velocities in Fig. 5b are roughly double that in Fig. 5a. The radial flow velocity near the contact line ($0.8 < R$) decreases to under 5 µm/s more quickly than that in the middle at $c_{av} < 0.2$. Self-pinning then occurred around $c_{av} = 0.23$. The flow velocity at $0.6 < R < 0.7$ also decreased until it was too small to measure at $c_{av} \geq 0.3$. In contrast, the fluid flow in the middle of the droplet ($R < 0.6$) obviously continues until at least $c_{av} = 0.5$, even after self-pinning. In Fig. 6b, there is a large difference between the measured film profiles and spherical cap in the middle, but little difference near the periphery of the film, where the flow velocity was under 5 µm/s before self-pinning or $c_{av} \leq 0.3$. That is, the solute distribution corresponding to the rim area ($0.6 < R \leq 1$) of the film is not affected by the continuous flow at $c_{av} \geq 0.3$; the continuous flow in the middle of the droplet after self-pinning primarily affects only the fine structure in the middle of the film. It is interesting that the absolute differences between the radial velocities of the outward flow ($u_R > 0$) on the free surface and inward flow ($u_R < 0$) near the bottom of the droplet in Fig. 5a, b, which imply the average amount of solute transferred to the contact line, are almost same order, while their film morphologies are quite different. The evaporative flux near the contact line increases with vapor pressure, which is adjusted by modulating the distance between the substrate and inkjet nozzle in this study. Thus, when the net amount of solute transferred to the contact line is constant, the solute accumulates faster with increasing evaporation rate, resulting in a decrease of the average mass fraction at self-pinning $c_{av,pin}$.

Figure 5c depicts the radial velocity profiles in a droplet on an R_f surface resulting in a nearly flat film like that shown in Fig. 6c. Initially, thermal Marangoni flow strongly dominates in the droplet; thus the absolute value of inward flow velocity ($u_R < 0$) on the free surface is larger than that of outward flow ($u_R > 0$) near the bottom of the droplet. The radial flow velocity quickly decreased, becoming zero near $c_{av} = 0.05$, which is probably because the solutal Marangoni force increases and balances with the thermal Marangoni

forces there. Thereafter, the solutal Marangoni force increases further until the outward flow on the free surface fully develops near $c_{av} = 0.07$. The radial flow velocity in the middle of the droplet ($0.2 < R < 0.3$) decreased to under 5 µm/s at $c_{av} < 0.3$. Then, the radial flow velocity at $R > 0.6$ decreased until it was too small to measure at $c_{av} \leq 0.33$. In Fig. 6c, the amount of solute corresponding to the difference between the measured film profiles and spherical cap near the apex probably caused by the internal flow at $c_{av} \leq 0.3$, at least not at $c_{av} > c_{av,pin}$, was 0.42. Because the overall internal flow velocity was already small at $c_{av} = 0.3$, the solute distribution did not change at $c_{av} > 0.3$.

It can be concluded from the above results that self-pinning and the strength of outward flow on the free surface at $c_{av} \leq 0.3$ or $\mu \leq 2.3$ Pa s determine the final film morphology. The solute distribution corresponding to the basic film structure that classified the film morphologies, such as the rim areas in ring-like films and convex trough in dot-like films, has already developed at self-pinning. The outward flow after self-pinning only affects the fine structure of the film, unless strong Marangoni flow, which is caused by heating of the substrate, multiple solvents, and surfactant, continues in the middle of the droplet after self-pinning.

3.4 Correlation of film morphology with Marangoni number

To quantify the effects of contact angles and evaporation rates on film morphology, self-pinning was further explored. According to the findings in Sect. 3.3, the amount of solute near the contact line is fixed before self-pinning. Thus, the mass fraction profiles near the contact line can be reasonably estimated from the ratio of measured film thickness to the droplet height at self-pinning. Figure 7 shows the radial profiles of mass fraction $c_{A,R}$ at self-pinning. For the ring-like film [denoted (b)], $c_{A,R}$ at $R < 0.7$ is not shown because the
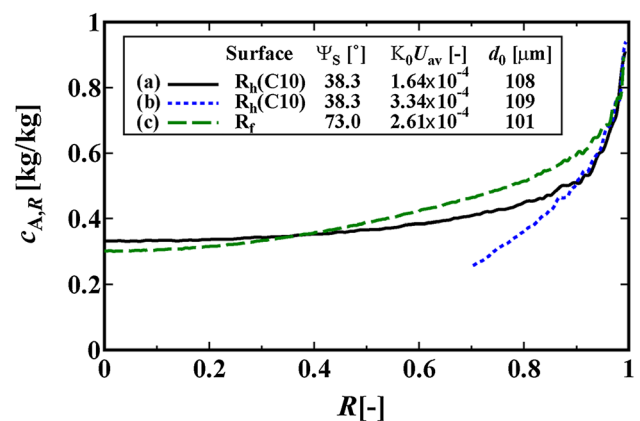

Surface	Ψ_S [°]	$K_0 U_{av}$ [-]	d_0 [µm]
(a) R_h(C10)	38.3	1.64×10^{-4}	108
(b) R_h(C10)	38.3	3.34×10^{-4}	109
(c) R_f	73.0	2.61×10^{-4}	101

Fig. 7 Profiles of mass fraction at self-pinning at different contact angles and the average evaporation volume rate

continuous flow remaining at $R < 0.7$ after self-pinning may affect $c_{A,R}$. Although $c_{A,R=1}$ cannot be determined because of division by zero, it is very interesting that $c_{A,R}$ of film (a–c) overlap at $R > 0.9$ and converge to 1 at self-pinning, irrespective of the film morphology. In other words, self-pinning, which happens when $c_{A,R}$ near the contact line is approximately one, is independent of the contact angle and evaporation rate.

Because the contact angle and evaporation rate change the strength of Marangoni flows, solutal and thermal Marangoni numbers are reasonable parameters to correlate with the effects of the contact angle and evaporation rate and the change of film morphology in this study. Eales et al. (2015) experimentally and theoretically correlated film morphology with Capillary number and the initial mass fraction in pinned droplets, but solutal and thermal Marangoni effects did not occur in their system.

When we use the same governing equations as those in a previous study (Yasumatsu et al. 2012), but choose a different characteristic concentration as $1 - c_A$, the solutal Marangoni number Ma_S is differently defined. Ma_S and also the thermal Marangoni number Ma_T were established as follows according to the method described in the "Appendix".

$$Ma_S = \frac{d\frac{\partial\gamma}{\partial c_A}\Delta c_A}{\mu\alpha}. \tag{2}$$

$$Ma_T = \frac{d\frac{\partial\gamma}{\partial T}\Delta T}{\mu\alpha}. \tag{3}$$

$$\Delta c_A = \frac{d(1 - c_A)\ddot{m}}{\rho D_{AB}}. \tag{4}$$

$$\Delta T = \frac{dL\ddot{m}}{k}. \tag{5}$$

$$\ddot{m} = \frac{f(\Psi_c)c_v D_v}{d}. \tag{6}$$

where d is the characteristic diameter, which is the same as the droplet diameter here, and $\ddot{m}$ is the evaporation flux at the droplet apex. c_v is solvent vapor density, and D_v is the diffusion coefficient in the gas phase. $f(\Psi_c)$ is a function of the contact angle, as shown in the "Appendix", and is constant in this study. $\ddot{m}$ in a saturated vapor atmosphere is conveniently estimated by Eqn. (6). In this study, the local vapor pressure of the solvent, which was controlled by the distance between the substrate and inkjet nozzle, was not easy to measure. Thus, $\ddot{m}$ was experimentally determined from the time variation of the droplet height and wetting

diameter. α is thermal diffusivity in the droplet. Δc_A and ΔT are, respectively, the characteristic mass fraction difference and temperature difference between the droplet apex and contact line. Physical properties at 298 K are thermal conductivity $k = 0.145$ J/(msK), heat capacity $C_p = 1840$ J/(kgK), and latent heat vaporization $L = 4.35 \times 10^{-5}$ J/kg. Empirical equations of surface tension gradient by temperature $\partial\gamma/\partial T = -1.2 \times 10^{-4}$ N/(mK), surface tension gradient by concentration $\partial\gamma/\partial c_A = 5.82 \times 10^{-2} c_A$ N/m/(kg/kg), viscosity $\mu = \exp(19.97 c_A - 5.16)$ Pa s, and density $\rho = 85.5 c_A + 989.4$ kg/m^3 were used. In general, the free volume theory proposed by Vrentas and Duda (1977) is used to predict the mass diffusion coefficient D_{AB} in concentrated polymer solutions. In this study, D_{AB} was set as a constant estimated using the equation proposed by Wilke and Chang (1955) with the pure solvent viscosity at 298 K. This is reasonable because the mass diffusion coefficient is almost a constant at semi-dilute concentration (Zettl et al. 2009), where the average mass fraction at self-pinning is. We set $c_{av} = c_{av,pin}$ and $d = d_{pin}$ from the experimental measurements and inserted them into Eqs. (1)–(5) to yield the solutal and thermal Marangoni numbers at self-pinning (denoted $Ma_{S,pin}$ and $Ma_{T,pin}$, respectively). Here, $1 - c_{av,pin}$ in $Ma_{S,pin}$ has the physical meaning of the driving force of the solutal Marangoni effect.

To correlate $Ma_{S,pin}$ and $Ma_{T,pin}$ with film morphology, $\Delta h/h_{cap}$ was defined, as shown in Fig. 8a. Δh is the difference between the spherical cap height h_{cap} with $d_{c,pin}$ and the center thickness h_{av} of the experimental film. In Fig. 8b, if the cylindrical shape is an ideal flat film, the volume and $d_{c,pin}$ are as same as those of the spherical cap, and the ratio of cylinder height and spherical cap height h_{cy}/h_{cap} is geometrically given by.

$$\frac{h_{cy}}{h_{cap}} = \frac{1}{2} + \frac{1}{6}\tan^2\left(\frac{\Psi_{cap}}{2}\right). \tag{7}$$

For a film formed on a substrate surface of $0 \le \Psi_S \le 90°$, the maximum h_{cy}/h_{cap} is 0.67 at $\Psi_{cap} = \Psi_{c,0} = 90°$ and $c_{av,pin} = 1$. In most cases, $\Psi_{cap} \ll \Psi_{c,0}$ and $c_{av,pin} \ll 1$; thus, film morphologies with h_{cy}/h_{cap} of ~0.5 indicate a nearly flat film. Accordingly, the film morphologies with $\Delta h/h_{cap} \gg 0.5$, $\Delta h/h_{cap} \sim 0.5$, and $\Delta h/h_{cap} \ll 0.5$ are ring-like, nearly flat, and dot-like, respectively. This definition is probably not valid for films produced by buckling instabilities (Pauchard and Allain 2003; Willmer et al. 2010).

The time variations of droplet height and wetting diameter on R_h(C10) and R_f surfaces were measured for multiple droplets to determine $Ma_{S,pin}$ and $Ma_{T,pin}$. A number of film morphologies were examined to calculate $\Delta h/h_{cap}$. Figure 9 shows the relationship between $Ma_{S,pin}$ and $\Delta h/h_{cap}$. Because $Ma_{T,pin}$ is 20–30 times smaller than $Ma_{S,pin}$ at room temperature, the effect of $Ma_{T,pin}$ on $\Delta h/h_{cap}$ was neglected here.
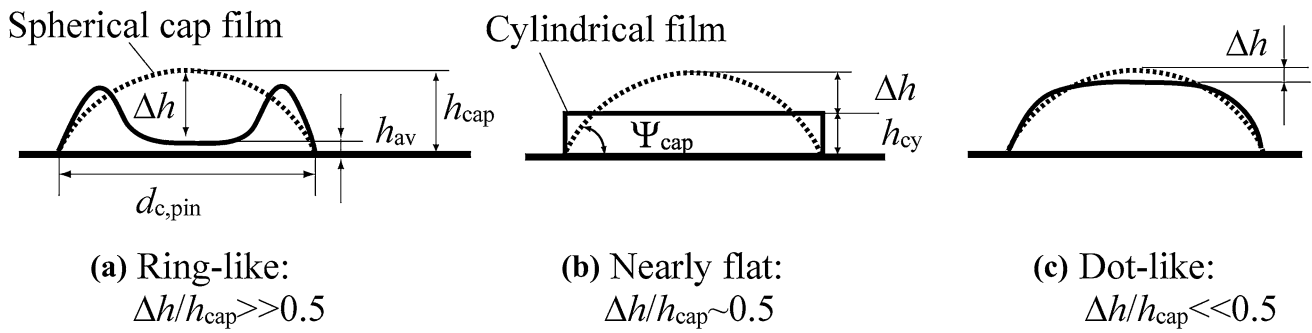
Fig. 8 Schematics illustrating the definitions of film morphologies; **a** ring-like, **b** nearly flat, and **c** dot-like
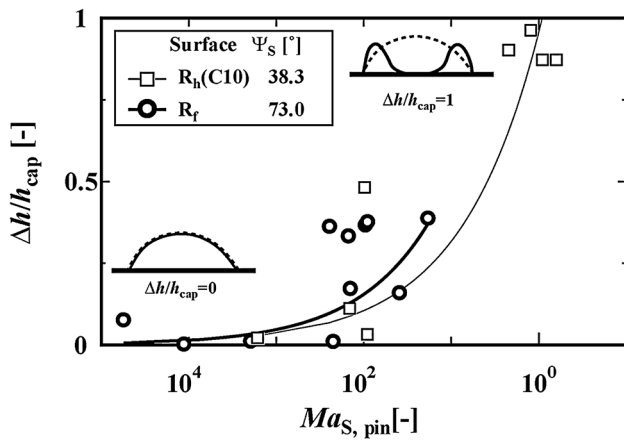

Fig. 9 Relationships between solutal and thermal Marangoni numbers and film morphology

In Fig. 9, $\Delta h/h_{cap}$ increases with $Ma_{S,pin}$; thereby, the dot-like film changes to a ring-like film with increasing solutal Marangoni flow. In Fig. 10, the film profiles are compared with $Ma_{S,pin}$. When $Ma_{S,pin}$ values are almost the same for systems with the different contact angles and average evaporation volume rates, the film morphologies in Fig. 10a, b is similar and the values of $\Delta h/h_{cap}$ are almost the same. This result suggests that it may be possible to control film morphology practically through $Ma_{S,pin}$ at room temperature. Yasumatsu et al. (2012) suggested that solutal and thermal Marangoni flows in droplets on heated substrate become competitive even after self-pinning. Both $Ma_{S,pin}$ and $Ma_{T,pin}$ should be related with film morphology and $\Delta h/h_{cap}$ in the future.

4 Conclusions

We experimentally visualized the internal flow inside PS–anisole droplets during solid film formation by inkjet printing at room temperature (298 ± 1 K). The effects of
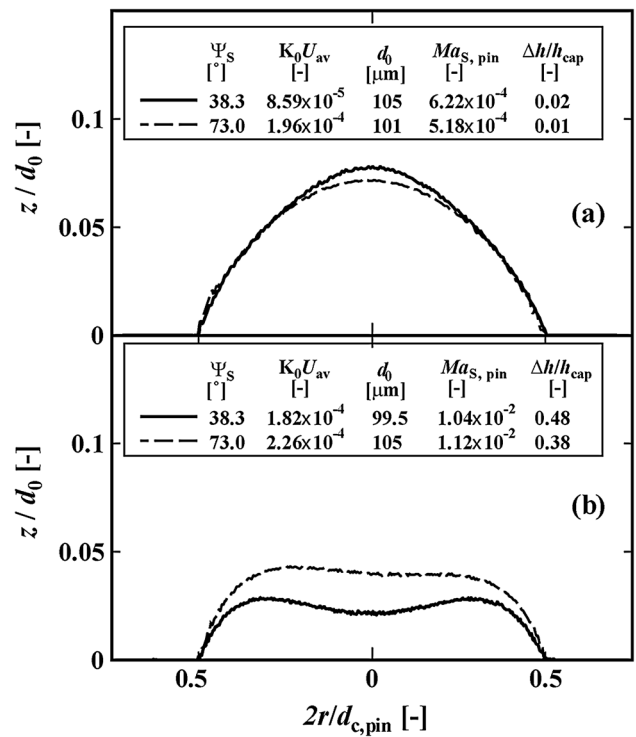

Fig. 10 Comparison of film profiles with solutal Marangoni number. These films were formed on the different substrate surfaces at average evaporation volume rates

contact angle ($\Psi_s = 38.3°$, 73°) and evaporation rate on the internal flow in droplets and resultant film morphology were quantitatively examined. The relationships between the radial flow velocity profiles and the average mass fraction, film morphology, and self-pinning were investigated to clarify the transport process during film formation. The solutal Marangoni number during the evaporation of a polymer solution droplet was defined to correlate with film morphology. The major findings are summarized as follows.

A change in the flow direction from inward to outward on the free surface was observed irrespective of the contact angle. The change of internal flow direction was reasonably

explained by the combination of solutal and thermal Marangoni effects. At room temperature, the thermal Marangoni effect is eventually overwhelmed by the solutal Marangoni effect at $c_{av} < 0.1$, and the solute is principally distributed by the outward flow, irrespective of the contact angles and average evaporation rate. Self-pinning and the strength of outward flow on the free surface at $c_{av} \leq 0.3$ or $\mu \leq 2.3\,\text{Pa s}$ determine the film morphology. The solute distribution corresponding to rim areas in ring-like films and the convex trough in dot-like films has already developed at self-pinning. The outward flow after self-pinning only affects the fine structure of the film, unless the strong Marangoni flow, which is caused by heating of the substrate, multiple solvents, and surfactant, continues in the middle of the droplet after self-pinning.

Fluid flow close to the contact line became too weak not to increase the amount of solute there after self-pinning. Consequently, the mass fraction profile at self-pinning was reasonably estimated by the droplet and film profiles. As a result, the mass fraction at the contact line $c_{A,R=1}$ converged to 1 regardless of the film morphology. This implies that self-pinning is independent of parameters such as the contact angle and evaporation rate.

The solutal and thermal Marangoni numbers at self-pinning, $Ma_{S,pin}$ and $Ma_{T,pin}$ were experimentally estimated for a number of droplets with different contact angles and evaporation volume rates. $Ma_{T,pin}$ was always 20–30 times smaller than $Ma_{S,pin}$ at room temperature; thus, the outward flow caused by the solutal Marangoni effect on the free surface dominates in the droplet before self-pinning. The film morphology or thickness variation $\Delta h / h_{cap}$ produced from droplets with different contact angles and the average evaporation volume rate were similar to each other when their $Ma_{S,pin}$ values were almost the same. This suggests that film morphology may be technically controlled by $Ma_{S,pin}$ at room temperature.

Appendix

The boundary conditions on the free surface of an evaporating droplet on a substrate are given by

$$-\mu \frac{\partial v_t}{\partial n} = \left(\frac{\partial \gamma}{\partial s} \right) = \left(\frac{\partial \gamma}{\partial T} \right) \frac{\partial T}{\partial s} + \left(\frac{\partial \gamma}{\partial c_A} \right) \frac{\partial c_A}{\partial s}. \tag{8}$$

$$-k \frac{\partial T}{\partial n} = \ddot{m} L. \tag{9}$$

$$-D_{AB} \frac{\partial c_A}{\partial n} = \frac{\ddot{m}}{\rho} c_A. \tag{10}$$

where v_t is tangential velocity, and n and s are coordinates normal and tangential to the free surface, respectively. T is temperature, k is thermal conductivity, L is latent heat vaporization, D_{AB} is mass diffusivity in the droplet, and ρ is density. The evaporative flux at the droplet apex $\ddot{m}$, which was proposed by Hu and Larson (2006), is given by

$$\ddot{m} = \frac{f(\Psi_c) c_v D_v}{d}. \tag{11}$$

$$f(\Psi_c) = \left(0.27 \Psi_c^2 + 1.3 \right) \left[1 - \left\{ 0.2239 \left(\Psi_c - \frac{\pi}{4} \right)^2 + 0.3619 \right\} \right]$$
$$\times \left\{ \tan\left(\frac{\Psi_c}{2} \right) \left(3 + \tan^2\left(\frac{\Psi_c}{2} \right) \right) \right\}^{\frac{1}{3}}. \tag{12}$$

When the characteristic velocity $v_0 = d/\alpha$, where d is the droplet diameter and α is thermal diffusivity, and the characteristic mass fraction $1 - c_A$ are selected, the normalized Eqn. (13) is obtained by substituting (9)–(11) into (8). Thus, thermal and solutal Marangoni numbers are defined:

$$\frac{\partial V_t}{\partial N} = \frac{d^2}{\mu \alpha} \left(\frac{\partial \gamma}{\partial s} \right) = \frac{d^2}{\mu \alpha} \left\{ \left(\frac{\partial \gamma}{\partial T} \right) \frac{\ddot{m} L}{k} \frac{\partial T}{\partial S} + \left(\frac{\partial \gamma}{\partial c_A} \right) \frac{\ddot{m}(1 - c_A)}{\rho D_{AB}} \frac{\partial c_A}{\partial S} \right\}$$
$$= \left\{ \frac{d \left(\frac{\partial \gamma}{\partial T} \right) \frac{f(\Psi_c) c_v D_v L}{k}}{\mu \alpha} \right\} \frac{\partial T}{\partial S}$$
$$+ \left\{ \frac{d \left(\frac{\partial \gamma}{\partial c_A} \right) \frac{f(\Psi_c) c_v D_v (1 - c_A)}{\rho D_{AB}}}{\mu \alpha} \right\} \frac{\partial c_A}{\partial S}$$
$$= Ma_T \frac{\partial T}{\partial S} + Ma_S \frac{\partial c_A}{\partial S}, \tag{13}$$

where V_t is the dimensionless tangential velocity, and N and S are the dimensionless coordinates normal and tangential to the free surface, respectively.

References

Bhardwaj B, Fang X, Attinger D (2009) Pattern formation during the evaporation of a colloidal nanoliter drop a numerical and experimental study. New J Phys 11:075020–075052. https://doi.org/10.1088/1367-2630/11/7/075020

Cummins G, Desmulliez MPY (2012) Inkjet printing of conductive materials: a review. Circuit World 38:193–213. https://doi.org/10.1108/03056121211280413

Deegan RD, Bakajin O, Dupont TF, Huber G, Nagel SR, Witten TA (1997) Capillary flow as the cause of ring stains from dried liquid drops. Nature 389:827–829. https://doi.org/10.1038/39827

Deegan RD, Bakajin O, Dupont TF, Huber G, Nagel SR, Witten TA (2000) Contact line deposits in an evaporating drop. Phys Rev E 62:756–765. https://doi.org/10.1103/PhysRevE.62.756

Eales AD, Routh AF, Dartnell N, Goddard S (2015) Evaporation of pinned droplets containing polymer—an examination of the important groups controlling final shape. AIChE J 61:1759–1767. https://doi.org/10.1002/aic.14777

Fukai J, Ishizuka H, Sakai Y, Kaneda M, Morita M, Takahara A (2006) Effects of droplet size and solute concentration on drying process of polymer solution droplets deposited on homogeneous surfaces. Int J Heat Mass Transf 49:3561–3567. https://doi.org/10.1016/j.ijheatmasstransfer.2006.02.049

Hu H, Larson RG (2006) Marangoni effect reverses coffee-ring depositions. J Phys Chem B 110:7090–7094. https://doi.org/10.1021/jp0609232

Kajiya T, Kaneko D, Doi M (2008) Dynamical visualization of coffee stain phenomenon in droplets of polymer solution via fluorescent microscopy. Langmuir 24:12369–12374. https://doi.org/10.1021/la8017858

Kaneda M, Ishizuka H, Sakai Y, Fukai J (2007) Film formation from polymer solution using inkjet printing method. AIChE J 53:1100–1108. https://doi.org/10.1002/aic.11154

Kaneda M, Hyakuta K, Takao Y, Ishizuka H, Fukai J (2008) Internal flow in polymer solution droplets deposited on a lyophobic surface during a receding process. Langmuir 24:9102–9109. https://doi.org/10.1021/la801176y

Komuro N, Takaki S, Suzuki K, Citterio D (2013) Inkjet printed (bio) chemical sensing devices. Anal Bioanal Chem 405:5785–5805. https://doi.org/10.1007/s00216-013-7013-z

Larson RG (2014) Transport and deposition patterns in drying sessile droplets. AIChE J 60:1538–1571. https://doi.org/10.1002/aic.14338

Morita M, Yasutake S, Ishizuka H, Fukai J, Takahara A (2005) Site-selective coating of polymer thin film prepared by the ink-jet method on the patterned fluoroalkylsilane monolayer substrate. Chem Lett 34:916–917. https://doi.org/10.1246/cl.2005.916

Pauchard L, Allain C (2003) Stable and unstable surface evolution during of a polymer solution drop. Phys Rev E 68:052801. https://doi.org/10.1103/PhysRevE.68.052801 **(05281–05284)**

Sefiane K (2014) Patterns from drying drops. Adv Coll Interface Sci 206:372–381. https://doi.org/10.1016/j.cis.2013.05.002

Su YJ, Yang WJ, Kawashima G (1988) Natural convection in evaporating sessile drops with solidification. Int J Heat Mass Transf 31:375–385. https://doi.org/10.1016/0017-9310(88)90020-8

Sun J, Bao B, He M, Zhou H, Song Y (2015) Recent advances in controlling the depositing morphologies of inkjet droplets. Appl Mater Interf 7:28086–28099. https://doi.org/10.1021/acsami.5b07006

Vrentas JS, Duda LJ (1977) Diffusion in polymer—solvent systems. I. Reexamination of the free-volume theory. J Polym Sci 15:403–416

Wilke CR, Chang P (1955) Correlation of diffusion coefficients in dilute solutions. AIChE J 1:264–270

Willmer D, Baldwin KA, Kwartnikab C, Fairhurst DJ (2010) Growth of solid conical structures during multistage drying of sessile poly(ethylene oxide) droplets. Phys Chem Chem Phys 12:3998–4004. https://doi.org/10.1039/b922727j

Yasumatsu S, Nakaso K, Fukai J (2012) Marangoni flows in polymer solution droplets drying on heating surfaces. J Chem Eng Jpn 45:128–135. https://doi.org/10.1252/jcej.11we124

Zettl U, Hoffmann TH, Koberling F, Krausch G, Enderlein J, Harnau L, Ballauff M (2009) Self-diffusion and cooperative diffusion in semidilute polymer solutions as measured by fluorescence correlation spectroscopy. Macromolecules 42:9537–9547. https://doi.org/10.1021/ma901404g

Zhang N, Yang WJ (1983) Evaporative convection in minute drops on a plate with temperature gradient. Int J Heat Mass Transf 26:1479–1488. https://doi.org/10.1016/S0017-9310(83)80048-9